Nature Communications

https://doi.org/10.1038/s41467-026-71015-9

Article in Press

Oriented diffusion tailors interfacial strain-polarization coupling for broadband electromagnetic absorption

Received: 17 October 2025

Accepted: 7 March 2026

Cite this article as: Rao, L., Zhao, X., Wang, X. *et al.* Oriented diffusion tailors interfacial strain-polarization coupling for broadband electromagnetic absorption. *Nat Commun* (2026). https://doi.org/10.1038/s41467-026-71015-9

Longjun Rao, Xuebing Zhao, Xinglong Wang, Bicheng Li, Chang Zhang, Guanyu Chen, Chongyun Liang, Wenbin You, Zhengchen Wu, Lei Wang & Renchao Che

Oriented diffusion tailors interfacial strain-polarization coupling for broadband electromagnetic absorption

Longjun Rao[1, 2, 3], Xuebing Zhao[1, 2, 3], Xinglong Wang[4, 5], Bicheng Li[1, 2, 3], Chang Zhang[1, 2, 3], Guanyu Chen[1, 2, 3], Chongyun Liang[1, 2, 3], Wenbin You[1, 2, 3], Zhengchen Wu[4], Lei Wang[4, *], Renchao Che[1, 2, 3, *]

[1] Laboratory of Advanced Materials, College of Smart Materials and Future Energy, Fudan University, Shanghai 200438, China

[2] Shanghai Key Lab of Molecular Catalysis and Innovative Materials, Fudan University, Shanghai 200438, China

[3] State Key Laboratory of Coatings for Advanced Equipment, Fudan University, Shanghai 200438, China

[4] School of Materials Science and Engineering, Tongji University, Shanghai 201804, China

[5] School of Materials Science and Engineering, University of Jinan, Jinan 250022, China

* Corresponding Authors.

Corresponding Authors' Emails: lei_wang@tongji.edu.cn (L. W.); rcche@fudan.edu.cn (R. C.)

Abstract

Repurposing the interfacial strain from a hindrance to synergism empowers critical advances for magnetoelectric composites in the application of next-generation energy storage and electromagnetic devices, by reconstructing the interfacial activity and local field distributions. However, its deterministic creation, pivotal for optimizing interfacial electron transport and emergent functionality, is impeded by the uncontrollable atomic distortion and arrangement. Here, we report an oriented-diffusion strategy that tailors interfacial strain by orchestrating atomic migration within a carbon-confined Fe_3C/ZnO magnetoelectric heterointerface. Engineering the outward effusion of dielectric ZnO generates a progressive strain gradient, driving a transition in the interfacial strain from compressive to tensile prior to eventual relaxation. This programmed strain state reconfigures atomic-scale electric fields at the heterointerface, thereby enhancing electron transports and interfacial polarization properties. Consequently, this enhancement enables the strain-mediated metamaterial outperforms conventional electromagnetic absorbers, exhibiting an ultrabroad effective absorption bandwidth covers the wireless communication and radar stealth spectra (2.0-18.0 GHz) with an over 95% radiation reduction. These findings provide a novel perspective on deciphering strain-polarization coupling mechanism and guide the development of advanced broadband magnetoelectric functional materials.

Keywords: Strain effect; Interfacial polarization; Atomic electric field; Magnetoelectric coupling; Electromagnetic wave absorption

Introduction

With the rapid advancement and widespread adoption of Internet of Things (IoT), artificial intelligence (AI), and smart mobile devices, the societal demand of wireless communication technologies has escalated to unprecedented heights[1,2]. However, less than 30% electromagnetic (EM) waves are utilized in telecommunication, the rest are largely ignored and wasted, constituting severe EM pollution in the surrounding environment and causing health concern and signal interference in electrical equipment[3]. EM absorption materials provide an effective solution to this issue by harvesting the EM wave and dissipating it into thermal energy. This fundamental energy-dissipation mechanism endows them with EM protection capability as functional fillers, enabling versatile applications that span from micro-nano high-precision electronics (such as on-chip components and integrated modules)[4] to large-scale architectural infrastructures[5, 6] (such as hospitals, laboratories, and transportation hubs) for industrial interference suppression and environmental shielding. Theoretically, the EM attenuation mechanism is mainly originated from the dielectric and/or magnetic dipoles of a material that interact with the radiation. To pursue superior absorption properties, considerable effort has been devoted to ingeniously integrating dielectric and magnetic components to achieve magnetic-dielectric coupling[7]. However, current research of magnetic/dielectric composites-based absorber attributes their synergistic effect to merely superimposing magnetic/dielectric contributions, ignoring the intrinsic interaction across the combined components[8,9]. Deciphering the potential magnetoelectric coupling mechanism for EM dissipation is heavily influenced by numerous factors (e.g., reasonable selection of materials system and systematical characterization), posing significant difficulty.

Designing magnetoelectric heterojunction is an effective approach to maximize the interaction between dielectric and magnetic components through a stable bonding at their contacted interface[10]. The heterogeneous interface, serves as a key mediator for magnetoelectric coupling, triggering distinctive interfacial effect such as built-in electric field, further contributing interfacial[11], or dipoles polarization, internal scattering for EM dissipation[12,13]. Interfacial strain commonly exists in the magnetoelectric heterointerface owing to the formation of chemical bonds and electrostatic

absorption across the interface[14]. Most reports roughly ascribe the contribution of strain for EM loss to dipole polarization induced by lattice defects and interfacial atoms rearrangement, while ignoring strain modulation towards the intrinsic electronic structure[15]. In certain dielectrics (e.g., piezoelectric, ferroelectric materials), residual static stress can trigger intrinsic electric polarization[16], leading to energy band bending, barrier height modulation, and electron-hole compensation[17]. Zinc oxide (ZnO) exemplifies this class of functional dielectrics, exhibiting inherent piezoelectric and semiconductor properties[18,19]. Its pronounced high-temperature thermodynamic instability, which drives distinctive thermal diffusion behavior[20], offers a practical pathway to leverage component rearrangement in designing interfacial interaction in the heterostructure systems. These findings establish magnetoelectric heterostructures as promising candidate materials for advanced electronic and spintronic applications, where interfacial strain can be regulated and potentially affect carrier transport efficiency. However, precise strain modulation at heterointerfaces, especially at the atomic scale, remains challenging. The difficulty mainly stems from the inherent lattice mismatch[21], thermal expansion incompatibility[22], and dynamic stress relaxation[23] during material synthesis, compounded by a lack of visualized analysis regarding strains-induced electronic structure transitions at the heterointerface. These inabilities impose huge obstacles on understanding the relationships between microscale interfacial strain and macroscale EM properties, severely restricting the deterministic strain regulation (including strain types and gradient) and the development of advanced EM functional heterostructures.

In this study, we demonstrated a programmed strain-polarization coupling mechanism and fabricated strain-controllable magnetoelectric interfaces by controlling oriented diffusion in carbon confined heterostructures. The interfacial strain transitioned sequentially from compressive to tensile and finally to a relaxed state during the outward diffusion of ZnO. This strain evolution mediated a volcano-type profile in interfacial coupling strength by reconstructing the electronic field distribution. Remarkably, engineering tensile strain at the magnetoelectric heterointerface effectively enhanced the electron transport and amplified the built-in electric fields, boosting interfacial polarization relaxation to dissipate the incident EM wave. The strain-polarization

coupled magnetoelectric metamaterial exhibits full-bandwidth (2-18 GHz) effective EM energy absorption, establishing it as a promising candidate for diverse applications in wide-frequency wireless communications and EM protection. Therefore, our work provided a novel method for designing magnetoelectric heterostructure with strong polarization responsiveness by leveraging interfacial strain, demonstrating significant potential for dual-use military and civilian applications.

Results and Discussion

Synthesis of confined magnetoelectric heterostructures

Confined ZnO/Fe_3C magnetoelectric heterostructures were fabricated by precisely diffusing ZnO nanoparticles to a specific depth within carbon frameworks (**Supplementary Fig. 1**). As shown in **Fig. 1a**, this process initiated with the transformation of carbonaceous substrate tethered Zn/Fe oxide (ZFO) hybrids into carbon encapsulated ZnO/Fe_3C yolk-shell nano-units through high-temperature carbothermal reduction, followed by manipulating the Zn source content for guiding the derivate ZnO effusion outwards the carbon nanocage. The carbon framework conversion from solid to yolk-shell was triggered by the Kirkendall cavitation effect[24], causing the creation of limited nanovoid, as evident by scanning electron microscopy (SEM) and transmission electron microscopy (TEM) images (**Supplementary Fig. 2**). As Zn source content increased, excess ZnO gradually filled the surrounding voids, eventually breached the carbon cages confinement, and diffused outward to form continuous ZnO layers. Consequently, the ZnO/Fe_3C (ZFC) heterostructure evolved through sequential confinement, penetration and separation stages with increasing ZnO content, as identified by high-resolution TEM (HRTEM), high-angle annular dark-field scanning transmission electron microscopy (HAADF-STEM) and energy-dispersive X-ray spectroscopy (EDS) elemental mapping (**Fig. 1b** and **Supplementary Fig. 3**), with the corresponding specimens termed ZFC-1, ZFC-2, and ZFC-3, respectively. Additionally, the augmented ZnO content enhanced the carbothermal reaction, as evident by the thermal gravity analysis (TGA) and Raman spectra (**Supplementary Fig. 4**), further boosting the gradient outward diffusion process.

In addition to morphology analysis, we performed *in-situ* argon ion sputtering to progressively

etch the outer ZnO layers of ZFC-3 to depths of up to 400 nm, thereby characterizing the outward diffusion affected component arrangements. X-ray photoelectron spectroscopy (XPS) depth profiling recorded both a gradual decrease in the intensity of characteristic Zn 2*p* peaks and an opposite trend in the Fe 2*p* signals (**Fig. 1c**), confirming the separation of ZnO and Fe_3C during the enhanced effusion process. Concurrently, the reaction between carbon substrates and ZFO induced the chemical transformation from $ZnFe_2O_4$ into ZnO and Fe_3C, resulting in the formation of an interface between ZnO and Fe_3C within the magnetoelectric heterostructures. The phase evolution and chemical state variation was verified by X-ray diffraction (XRD), X-ray absorption near edge structure (XANES), extended X-ray absorption fine structure (EXAFS), and XPS analysis (**Fig. 1d-e**, **Supplementary Fig. 5-8** and **Table 1**). The absorption edge of Fe *k*-edge of ZFO and ZFC samples were close to that of Fe_3O_4 and Fe, respectively. In the Fe *k*-edge EXAFS of ZFO, a shift towards higher radial distance was detected in the peak of characteristic Fe-O-Fe, further identifying the formation of $ZnFe_2O_4$ in ZFO[25]. Meanwhile, the EXAFS of ZFC also confirmed the presence of Fe_3C (via Fe-Fe and Fe-C peaks)[26] and indicated the formation of interfacial chemical bonds in Fe_3C/ZnO heterojunctions, as evident from emerging Fe-O peaks with a shift towards increased radial distance.

To reveal the configuration of the magnetoelectric interface built by semiconductor ZnO and ferromagnetic Fe_3C, an aberration-corrected HAADF-STEM was employed to capture the ZnO/Fe_3C heterostructures (**Fig. 1f**). Atomic arrangement of ZnO/Fe_3C revealed a feature of coherent heterointerface, where the ZnO presented the (101) crystal plane and Fe_3C exhibited the (211) crystal facet, thereby confirming atomically interactive connectivity across the interface. To minimize potential inaccuracies caused by closely spaced lattice, integrated differential phase contrast (iDPC) STEM was carried out. Detection of **Fig. 1g** presented a strong quantitative agreement between the crystalline structure and STEM results, accurately verifying the formation of magnetoelectric heterointerface between Fe_3C (211) and ZnO (101). Additionally, the distribution of the intrinsic atomic-scale electric fields within Fe_3C and ZnO were visualized using differential phase contrast (DPC) STEM[27], with color vector wheels indicating the direction of the

electric field (**Fig. 1h**). A uniform yet asymmetrical distribution of the local atomic electric field within each component reveals different potentials[28], potentially inducing built-in electric field at the magnetoelectric interface.

Diffusion-regulated interfacial strain in confined ME heterostructures

To provide insights into the correlation between ZnO diffusion and magnetoelectric interface contact, molecular dynamics (MD) simulation (**Supplementary Note 1**) was employed to elucidate the ZnO content affected effusion process. The observations of recorded diffusion state indicated that at lower concentrations, ZnO molecules were largely hindered from penetrating the carbon layers (**Fig. 2a**). Conversely, with a higher initial concentration, the confinement imposed by the carbon layers was progressively overwhelmed, leading a pronounced outward diffusion. Continuous increase of the number density of penetrated ZnO (**Fig. 2b** and **Supplementary Fig. 9**) and the mean-square displacement (MSD, **Fig. 2b**) with the augmented concentration further proved the controllability of the ZnO gradient effusion process. In addition, ZnO oriented migration process inevitably affected the interface state, inducing potential reconfiguration of interfacial strain at the heterointerface. The interfacial stress field resulted from the ZnO gradient diffusion was characterized using geometric phase analysis (GPA) of STEM, complemented by strain distribution statistics (**Fig. 2c-d** and **Supplementary Fig. 10**). At the primary stage of magnetoelectric interface formation (ZFC-1), about 10.2% compression strains were detected at the ZFC interface, which was originated from the bonding effect of heterostructure formation. Upon initiation of ZnO outward diffusion (ZFC-2), the excess ZnO filled the original nanovoid within the carbon nanocages and tended to separate out, thereby inducing traction from the outer carbon layers on the penetrated ZnO. Concurrently, the upcoming separation of ZnO was also constrained by Fe_3C owing to the interfacial bonding at the ZnO/Fe_3C coherent heterojunctions and the static absorption, resulting in significant tension strain (16.8%) at their atoms contacted interface. The enhanced outward diffusion of ZnO overcame the constrains of both carbon shells and the interfacial bonding, thereby triggering the dissociation of the original ZnO/Fe_3C heterointerface, as evident by the disappearance of Fe-O bond in Fe *k*-edge EXAFS of ZFC-3

(**Supplementary Fig. 11**). Seldom residual strain (0.5%) remained at the emerging Fe_3C-C-ZnO triple-phase interface. Thus, the gradient-oriented diffusion process effectively governed a programmatic progression of the interfacial strain state from compressive to tensile, ultimately leading to its relief. The same interfacial strain states, with comparable quantitative values, was consistently observed in ZFC-x specimens across different batches (**Supplementary Fig. 12**), confirming the reproducibility and controllability of the oriented diffusion strategy.

To decipher the strain affected interfacial electronic structure, the distributions of interfacial electric field under different strain state were analyzed by the DPC-STEM technique (**Fig. 2e**). Unlike the uniform atomic electric fields in a homogenous component, pronounced distortion and mutual interaction were observed between neighboring Fe and Zn atoms across the interface, providing direct evidence of electric field couplings at the magnetoelectric heterointerface[29]. This atomic-level interfacial electric coupling was more pronounced as the compression strain converted to the tensile strain at the interface, which could accelerate the carriers transport across the interface and enhanced interfacial polarization. In contrast, only continuous and symmetrical atomic electric fields was observed within the separated ZnO, with no detectable electric field reconfigurations at the interface, implying the interfacial decoupling in ZFC-3 owing to the extinction of magnetoelectric heterojunction. In addition, the strain-mediated evolution of the interfacial coupling was analyzed using vector field distribution[30] reconstructed from the atomic electric field maps (**Fig. 2f**). Characteristic gradients in the electric field vector rotation were detected at the magnetoelectric interfaces, confirming the strain-induced interfacial coupling. This coupling phenomenon was remarkably enhanced under tensile strain yet vanished upon interface separation. By precisely controlling ZnO diffusion to introduce interfacial strain, effectively programming the atomic electric field arrangement and the polarization capability at the magnetoelectric heterointerface.

Interfacial strain regulated electrical properties

The interfacial strain evolution guided by the gradient diffusion reconstructed the atomic interaction at the magnetoelectric heterointerface, varying the electrons motion in the interfacial

built-in electric field (BIEF), thereby affecting the related electrical properties. Dielectric dispersion, manifested in frequency-dependent permittivity, fundamentally originated from the dynamic dielectric loss of absorbers to an external alternating electric field[31]. The variation of permittivity revealed that the interfacial strain enhanced dielectric dispersion properties, as verified by a steeper decline in permittivity with increasing frequency (**Supplementary Fig. 13a-b**) and a broader variation range across the 2–18 GHz band (**Fig. 3a**). This enhancement was mainly due to the strain-induced reconstruction of the local electronic structure via interfacial coupling (**Fig. 2e-f**), which accelerated realignment of interfacial potentials across the interface in response to the altering electric field, thereby improving interfacial polarization responsiveness[32]. The enhanced polarization relaxation could be characterized by the decreased real permittivity (ε′) and a more intense dielectric resonance peak in the imaginary part (ε″) for the strain-involved specimen (**Supplementary Fig. 13a-b**). According to the non-ideal Debye relaxation model[33], the ε'', referred to the dielectric loss ability, was divided into conduction loss (ε_c'') and polarization relaxation (ε_p'') based on the tested electronic conductivity (**Supplementary Table 2** and **Supplementary Fig. 13c-d**). Multiple polarization peaks were identified in the strain-involved ZFC heterostructures, and both of the peak intensity and width were increased as the interfacial state evolved from the relieved to compressive and tensile. This enhancement was also confirmed by the loss tangent of complex permittivity ($\tan\delta_\varepsilon = \varepsilon''/\varepsilon'$), where the increased $\tan\delta_\varepsilon$ indicated the strain-improved dielectric loss ability (**Fig. 3b**). In addition, the interfacial strain affected polarization relaxation variation were analyzed by Cole-Cole plots. As the interfacial strain evolved from a relieved state to compressive and tensile states, the maximum relaxation peak shifted to higher frequencies (**Fig. 3b**), along with a broadened peak width (**Fig. 3c**). Theoretically, polarization relaxation peaks occurred when the frequency of the external electric field coincides with the intrinsic response rate (the reciprocal of the relaxation time) of the polarization mechanism within the absorbers[34]. Thus, this trend of relaxation peaks varied by the interfacial strain suggested a shortened relaxation time with a widened distribution[35], demonstrating a sensitive yet broadband dielectric loss capability in the strain-involved magnetoelectric heterostructure.

To reveal the strain state-regulated interfacial polarization loss capability, off-axis electron holograms and projected charge density maps are conducted (**Fig. 3d** and **Supplementary Fig. 14**). The red and bule regions in charge maps corresponded to the electronic depletion and accumulation, respectively, and the color depth reflected the charge density. The 3D charge density distribution of the strain-relieved interface exhibited flat distribution with weak intensity, ascribing to the decouple of the magnetoelectric interaction (**Fig. 2f**). In contrast, remarkable fluctuation characterized by the uneven arrangement of positive and negative charge were detected in the ZFC heterointerface with compression and tension strain. The increased potential differences implied the augmented absolute electronegativity across these coupled interfaces, which promoted interfacial polarization and its associated electric field energy dissipation. After a sequential process of Fast Fourier Transform (FFT), Inverse FFT (IFFT), filter method, the electron wave phases in the holograms were converted into electric potentials, finally the localized polarization intensity could be calculated based on the Poisson's equations[29]. **Fig. 3e** illustrated that interfacial strain effectively elevated the polarization intensity, which could be further enlarged by the tensile strain owing to the accelerated electrons transport by the enhanced interfacial coupling. Additionally, the $\varepsilon_p''/\varepsilon_c''$ value could reflect the contribution of polarization loss within the tested frequency range. As shown in **Fig. 3f**, the values of $\varepsilon_p''/\varepsilon_c''$ ratio rise with increasing frequency, indicating that polarization loss played a more dominant role at higher frequencies. Notably, this frequency dependent enhancement was most significant in the ZFC-2 specimen with interfacial tensile strain, highlighting the controllability of polarization loss through strain engineering.

To deeply decipher the regulation mechanism of the polarization loss, the reconfigured electronic structures in the ZnO gradient diffusion controlled ZFC-based heterointerfaces were further theoretically analyzed by density functional theory (**Supplementary Note 2**). The projected density of state (PDOS) analysis revealed a gradient diffusion-induced reconstruction of interfacial electronic structures (**Fig. 3g**) and BIEF, consistent with the observation from the DPC and electron holography. As tensile strain was formed on the ZFC heterointerface, more pronounced orbits overlaps were detected, assigning to the enhanced interfacial coupling interaction, thereby

boosting electron transports of the external electric field across the interface. As the interfacial strain state evolved from the relieved to compressive and tensile, the reduced work function (Φ) suggested the lowered energy barriers for charge migration (**Fig. 3h** and **Supplementary Fig. 15**), which improved the electron mobility and activity[36]. This improvement facilitated the supply of polarizable charges, thereby promoting the response of interfacial dipoles to external alternating electric fields. In additional, the differential charge density distribution revealed pronounced and inhomogeneous charge accumulation and depletion at these coupled magnetoelectric interfaces (**Supplementary Fig. 16**), forming multiple localized space-charge regions[34]. This result indicated the generation of robust interfacial dipole layers with a wide distribution[37], which could account for broadening the distribution of polarization relaxation. Thus, these combined experimental results and theoretical analyses revealed a tunable strain-polarization coupling mechanism. The interfacial strain evolution, tailored by oriented diffusion, effectively orchestrated a reconfiguration of interfacial electronic properties via constructing interfacial coupling. This process created intense and wide-ranging polarization responsiveness, thereby significantly enhancing the dielectric loss performance in response to the external EM wave.

Application in EM wave absorption

Owing to the strain-tailored interfacial electric coupling effects and enhanced electric properties, the Fe_3C/ZnO magnetoelectric heterostructures exhibited significant dielectric loss ability, showing potential application in efficient EM wave absorption. The strain-regulated EM absorption performance of the as-fabricated magnetoelectric heterostructures was evaluated, indexed by reflection loss (RL) and effective absorption bandwidth (EAB, frequency range of $RL \leq -10$)[38]. In **Fig. 4a** and **Supplementary Fig. 17**, both the minimum RL (RL_{min}) and maximum EAB (EAB_{max}) exhibited the optimum when the magnetoelectric interface was subjected to tensile strain. A detail analyses of the EM parameters and magnetic response properties evolution (**Supplementary Fig. 18-22** and **Note 3**) attributed this improvement to the increased dielectric loss ability caused by the strain-enhanced interfacial polarization and optimized impedance matching. The Fe_3C/ZnO heterostructure within tensile strain exhibited a broad EAB_{max} of 7.38

GHz, covering entire Ku-band (from 12 to 18 GHz, the primary application band for radar stealth[39]), outperforming most reported EM absorption materials (**Fig. 4b** and **Supplementary Table 3-4**). Furthermore, we employed finite element analysis to simulate the surface current density and radar cross section (RCS) of a perfectly electric conducting (PEC) plate coated with ZFC-based magnetoelectric composites layers (**Fig. 4c**, **Supplementary Fig. 23** and **Note 4**). Uniform distribution of surface current density[40] and significant RCS reduction[41] demonstrated the superior impedance matching and effective absorption properties of the strain-enhanced ZFC heterostructure in the simulated practical EM environment.

Widespread adoption of wireless communication techniques in civilian escalated the societal demand of absorbers with ultrawide EAB for addressing EM interference (produced by e.g., base stations, wireless routers and electronic devices)[42,43]. According to the equivalent medium theory, the periodic structure at subwavelength produced uniform EM response[44]. To achieve full-band absorption, an EM metamaterial was fabricated by mixing the strain-mediated Fe_3C/ZnO heterostructures with resin and molding it into an 18 × 18 cm periodic metastructure (**Supplementary Fig. 24** and **Table 5**), and the design principle of the metastructure were detailed in **Supplementary Note 4**. This hierarchical architecture, which featured pyramid-shaped units with internal perforation, could generate additional multiple resonances through impedance gradient matching and spatial dispersion. **Fig. 4d** showed the practical photos of the magnetoelectric metamaterial under the far-field testing environment. Remarkably, ultrawide EAB performance across the entire 2–18 GHz band was achieved, attributing to the synergistic effect between intrinsic excellent magnetoelectric coupling loss from heterostructures and diffraction resonances supplied by the metastructure.

To verify the application potential, we tested the absorption attenuation of the metamaterial against EM waves emitted by a 5G wireless router. Positioned as a shield in front of the WiFi router, the metamaterial remarkably reduced the detected radio frequency (RF) signals to the qualified levels (**Fig. 4e**). And the pronounced surface temperature elevation of the ZFC-2 metamaterials after radiation under a solid-state microwave source confirms the involved dissipation process

from absorbed EM energy to heat (**Supplementary Fig. 25** and **Fig. 4f**). Time dependent radiation values variation revealed that over 95% reduction of RF signals could be continuously achieved by this magnetoelectric metamaterials (**Fig. 4g**). In contrast, both control samples (the all-resin metastructure and the ZFC-2/resin plate) failed to achieve effective EM attenuation (**Supplementary Fig. 26**), further demonstrating that the impressive EM protection arises from the synergistic contribution between the strain-mediated magnetoelectric absorbers and the designed metastructure. Additionally, the corresponding dissipation mechanism was investigated via finite element simulation[45]. The frequencies (5.8 and 14.0 GHz) of characteristic resonance peaks identified from the RL results were selected to elucidate the EM field response behaviors. As shown in **Fig. 4h**, the attenuation of low-frequency EM energy occurred primarily through magnetic field dissipation, while at high frequencies it is dominated by electric field dissipation. This frequency-dependent behavior was confirmed by the spatial overlap of electric/magnetic field distributions and energy loss profiles[46]. These inspiring findings demonstrated that the tensile strain-enhanced magnetoelectric heterostructure provided a promising sustainable solution to address the elevating EM interference.

In conclusion, we have successfully fabricated carbon confined ZnO/Fe_3C magnetoelectric heterostructures, and precisely tailored the interfacial strain by controlling the oriented diffusion gradient. As the strain of the magnetoelectric heterointerface evolved from the compressive to the tensile and relieved, the interfacial atomic electric fields exhibited an evolution from the enhanced interfacial coupling to the decoupling. Furthermore, the strain-driven coupling effect reconfigured the electronic structures across the atomic heterointerface, effectively accelerating the interfacial electrons transport and broadening the distribution of interfacial dipoles, thereby enhancing the polarization relaxation response ability. Eventually, the tensile strain-enhanced magnetoelectric heterostructure performed impressive EMA properties with a broad EAB covered 7.38 GHz; and its derivate metamaterials achieved full-band efficient absorption (2-18 GHz) and over 95% radiation attenuation efficiency, exhibiting significant potential for dual-use civilian and military application. Our results proposed a novel mechanism of interfacial strain engineering in regulating

electronic properties and broaden the design paradigm of advanced EM functional materials.

Methods

General

The chemicals, electromagnetic parameters measurement, molecular dynamics simulation, and density functional theory are given in the Supplementary Methods and Notes.

Synthesis of ZnO/Fe_3C@C-x (ZFC-x)

ZFC-x microspheres were prepared by continuous spray drying and annealing treatment. First, 3.0 g PVP-K30 and 0.9 g TMA was dissolved in of a 60 mL solution composed of isometric DI water, anhydrous ethanol, and DMF under vigorous stirring to obtain a homogenous solution. Then, 2.0 mmol $Fe(NO_3)_3 \cdot 9H_2O$, x mmol $Zn(NO_3)_2 \cdot 6H_2O$ were simultaneously added into the solution and stirring until dissolution. The final obtained yellow spray solution was fed into a spray dryer, and the spray drying parameters were an inlet temperature of 180 °C, outlet temperature of 90 °C, feed rate of 1500 mL h^{-1}, and an atomization pressure of 0.4 bar. The collected spray dried precursors were pre-treated at 300°C for 60 min to obtain solid ZFO@C hybrids, followed by pyrolyzing at 600 °C under N_2 atmosphere for 300 min at a heating rate of 2 °C/min to obtain the ZFC-x. In addition, the ZFC-x samples prepared at the $Zn(NO_3)_2 \cdot 6H_2O$ amount of 1.0, 3.0, and 5.0 mmol were denoted as ZFC-1, ZFC-2, and ZFC-3, respectively.

Fabrication of ZFC based EM metamaterials

ZFC-based metamaterials with a size of 18 × 18 cm within periodic aligned units were prepared via a moulding process, the geometric parameters of the as-designed metamaterial unit were listed in **Supplementary Table 5**. First, a rubber inverted mold template was obtained via 3D printing. Then, a certain amount of ZFC powders were added into a fresh prefab resin mixture (the added weight ratios of resin E51, curing agent, and accelerator were 14:5:1) with a weight ratio of 2:3 and violently stirred for 30 min. The as-obtained ZFC/resin mixtures were poured into the 3D-printed inverted mold template and degassed for 60 min under the vacuum ambient. The inverted

mold template with the degassed ZFC/resin mixtures were transferred to an oven and cured under 80 ºC for 12h. After the completion of curing, the final ZFC-based EM metamaterial was obtained.

Characterization

Field-emission SEM images were obtained using a Hitachi S-4800 microscope. TEM, HRTEM, EDS mapping results and off-axis electronic holography results were obtained on a on a dual spherical aberration correction field-emission STEM (Thermo Fisher Scientific, Spectra 300 TEM, American) operated at 300 kV, equipped with STEM-iDPC detector, STEM-HAADF detector, and Super-X EDS. X-ray diffraction (XRD) patterns were recorded on a Bruker-Axe X-ray diffractometer equipped with a Cu Kα radiation source (λ = 1.5406 Å, 40.0 kV, 40.0 mA). X-ray photoelectron spectroscopy (XPS) results were analysed on a Thermo Scientific ESCALAB 250Xi spectrometer equipped with a monochromatic X-ray source and argon etching system. X-ray absorption fine structure spectra were collected at the RapidXAFS 2M (Anhui Absorption Spectroscopy Analysis Instrument Co., Ltd.) by transmission mode at 20 kV and 40 mA. All spectra were collected in ambient conditions. Raman spectroscopy measurement was performed on a Renishaw inVia spectrometer under a 633 nm laser excitation. Thermogravimetric analysis (TGA, PerkinElmer) was performed in an air atmosphere to evaluate the content variation. The conductivity of the samples was tested by analysis of a four-point probe surface resistance tester.

Data Availability

Source data are provided with this paper. The data that support the findings of this study are available from the corresponding author upon request.

References

1. Tao, Z. et al. Ultrabroadband on-Chip Photonics for Full-Spectrum Wireless Communications. *Nature* 1-8 (2025).
2. Han, S. & Bian, S. Energy-Efficient 5G for a Greener Future. *Nat. Electron.* **3**, 182-184 (2020).
3. Lv, H. et al. Staggered Circular Nanoporous Graphene Converts Electromagnetic Waves into Electricity. *Nat. Commun.* **14**, 1982 (2023).
4. Zhao, Z. et al. Advancements in Microwave Absorption Motivated by Interdisciplinary Research. *Adv. Mater.* **36**, 2304182 (2024).
5. Wang, X., Li, Q., Lai, H., Peng, Y., Hou, C., & Xu, S. A Bionic Grooving All-Cementitious-Dielectric Metastructure with Unprecedented Wide-Angle Broadband Electromagnetic Wave Absorption Properties. *Adv. Funct. Mater*. 2425949 (2025).
6. Lei, D. et al. A State-of-the-art on Electromagnetic and Mechanical Properties of Electromagnetic Waves Absorbing Cementitious Composites. *Cement Concrete Comp.* **157**, 105889 (2025).
7. Cai, B. et al. Interface-Induced Dual-Pinning Mechanism Enhances Low-Frequency Electromagnetic Wave Loss. *Nat. Commun.* **15**, 3299 (2024).
8. Liu, P. et al. Synergistic Dielectric–Magnetic Enhancement via Phase-Evolution Engineering and Dynamic Magnetic Resonance. *Adv. Funct. Mater.* **33**, 2211298 (2023).
9. Qu, N. et al. 2D/2D Coupled MOF/Fe Composite Metamaterials Enable Robust Ultra–Broadband Microwave Absorption. *Nat. Commun.* **15**, 5642 (2024).
10. Luo, B. et al. Magnetoelectric Microelectromechanical and Nanoelectromechanical Systems for the IoT. *Nat. Rev. Electr. Eng.* **1**, 317-334 (2024).
11. Liu, Q., Zhang, D. & Fan, T. Electromagnetic Wave Absorption Properties of Porous Carbon/Co Nanocomposites. *Appl. Phys. Lett.* **93** (2008).
12. Yang, H. et al. Enhanced Dielectric Properties and Excellent Microwave Absorption of SiC Powders Driven with NiO Nanorings. *Adv. Opt. Mater.* **2**, 214-219 (2014).

13. Liang, L. et al. Heterointerface Engineering in Electromagnetic Absorbers: New Insights and Opportunities. *Adv. Mater.* **34**, 2106195 (2022).

14. Li, T., Deng, S., Liu, H. & Chen, J. Insights into Strain Engineering: from Ferroelectrics to Related Functional Materials and Beyond. *Chem. Rev.* **124**, 7045-7105 (2024).

15. Zhang, S., Lan. D., Zheng, J., Zhao, Z., Jia, Z. & Wu, G. Insights into Polarization Relaxation of Electromagnetic Wave Absorption. *Cell Rep. Phys. Sci.* **5**, (2024).

16. Yu, Q. et al. Highly Sensitive Strain Sensors Based on Piezotronic Tunneling Junction. *Nat. Commun.* **13**, 778 (2022).

17. Miao, Y., Zhao, Y., Zhang, S., Shi, R. & Zhang, T. Strain Engineering: A Boosting Strategy for Photocatalysis. *Adv. Mater.* **34**, 2200868 (2022).

18. Wang, L. N., et al. Polarization Mechanism of Oxygen Vacancy and its Influence on Dielectric Properties in ZnO. *Chinese Phys. Lett.* **28**, 027101 (2011).

19. Yadav, R. S., & Kuřitka, I. Recent Advances on Outstanding Microwave Absorption and Electromagnetic Interference Shielding Nanocomposites of ZnO Semiconductor. *Adv. Colloid Interface Sci.* **326**, 103137 (2024).

20. Feng, X. et al. ZnOx Overlayer Confined on $ZnCr_2O_4$ Spinel for Direct Syngas Conversion to Light Olefins. *Nat. Commun.* **16**, 3711 (2025).

21. Wang, Y. et al. Lattice Mismatch at the Heterojunction of Perovskite Solar Cells. *Angew. Chem. Int. Ed.* **136**, e202405878 (2024).

22. Chavez-Angel, E. et al. Engineering Heat Transport Across Epitaxial Lattice-Mismatched van der Waals Heterointerfaces. *Nano Lett.* **23**, 6883-6891 (2023).

23. Zhang, Y., Si. W., Jia, Y., Yu, P., Yu, R. & Zhu, J. Controlling Strain Relaxation by Interface Design in Highly Lattice-Mismatched Heterostructure. *Nano Lett.* **21**, 6867-6874 (2021).

24. Fan, M., Liao, D., Aboud, M., Shakir, I. & Xu, Y. A Universal Strategy toward Ultrasmall Hollow Nanostructures with Remarkable Electrochemical Performance. *Angew. Chem. Int. Ed.* **132**, 8324-8331 (2020).

25. Bock, DC. et al. (De)Lithiation of Spinel Ferrites Fe_3O_4, $MgFe_2O_4$, and $ZnFe_2O_4$: a

Combined Spectroscopic, Diffraction and Theory Study. *Phys. Chem. Chem. Phys.* **22**, 26200-26215 (2020).

26. Liu, C. et al. Synergistic Catalysts with Fe Single Atoms and Fe_3C Clusters for Accelerated Oxygen Adsorption Kinetics in Oxygen Reduction Reaction. *Angew. Chem. Int. Ed.* **64**, e202501266 (2025).
27. Shibata, N. et al. Direct Visualization of Local Electromagnetic Field Structures by Scanning Transmission Electron Microscopy. *Acc. Chem. Res.* **50**, 1502-1512 (2017).
28. Xiong, X. et al. Atomic-Level Electric Polarization in Entropy-Driven Perovskites for Boosting Dielectric Response. *Adv. Mater.* **37**, 2415351 (2025).
29. Wu, Z. et al. Electrochemical Switching of Electromagnetism by Hierarchical Disorder Tailored Atomic Scale Polarization. *Adv. Mater.* **36**, 2410466 (2024).
30. Xu, J. et al. Atomic-Level Polarization in Electric Fields of Defects for Electrocatalysis. *Nat. Commun.* **14**, 7849 (2023).
31. Tao, J. et al. Phenolic Multiple Kinetics-Dynamics and Discrete Crystallization Thermodynamics in Amorphous Carbon Nanostructures for Electromagnetic Wave Absorption. *Nat. Commun.* **15**, 10337 (2024).
32. Lu, B. et al. Microwave Absorption Properties of the Core/Shell-type Iron and Nickel Nanoparticles. *J. Magn. Magn. Mater.* **320**, 1106-1111 (2008).
33. Lv, H., Yang, Z., Pan, H. & Wu, R. Electromagnetic Absorption Materials: Current Progress and New Frontiers. *Prog. Mater. Sci.* **127**, 100946 (2022).
34. Zhang K. et al. All-Dielectric Ultra-broadband Microwave Absorbing Aerogel with Optimized Dielectric Dispersion via Dielectric Relaxation Time Regulation. *Adv. Mater.* 2506386 (2025).
35. Puzenko, A., Ishai, P. B., & Feldman, Y. Cole-Cole Broadening in Dielectric Relaxation and Strange Kinetics. *Phys. Rev. Lett.* **105**, 037601 (2010).
36. Zhang, S. et al. New prospects in Built-in Electric Fields for Electromagnetic Wave Absorption: from Fundamentals to Interdisciplinary Applications. *Adv. Funct. Mater.*

e13762 (2025).

37. Tung, R. T. Electron Transport at Metal-Semiconductor Interfaces: General Theory. *Phys. Rev. B* **45**, 13509 (1992).

38. He, M. et al. Excellent Low-Frequency Microwave Absorption and High Thermal Conductivity in Polydimethylsiloxane Composites Endowed by Hydrangea-Like CoNi@ BN Heterostructure Fillers. *Adv. Mater.* **36**, 2410186 (2024).

39. Huang, Y., Chen, G., Wang, X., Ma, H. & Chai, C. Advances in Radar/Infrared Compatible Stealth Materials. *J. Mater. Sci. Mater. El.* **36**, 1-33 (2025).

40. He, P. et al. Hierarchical and Orderly Surface Conductive Networks in Yolk-shell Fe_3O_4@C@Co/N-doped C Microspheres for Enhanced Microwave Absorption. *Small* **19**, 2302961 (2023).

41. Zhang, X. et al. Metal-Organic Frameworks with Fine-Tuned Interlayer Spacing for Microwave Absorption. *Sci. Adv.* **10**, eadl6498 (2024).

42. Qu, S. Hou, Y. & Sheng, P. Conceptual-Based Design of An Ultrabroadband Microwave Metamaterial Absorber. *Proc. Natl. Acad. Sci. U. S. A.* **118**, e2110490118 (2021).

43. Zhang, Y. et al. Multifunctional Electromagnetic Wave Absorbing Carbon Fiber/Ti_3C_2TX MXene Fabric with Ultra-wide Absorption Band. *Carbon* **230**, 119594 (2024).

44. Zhang, T. et al. Polarization Insensitive Hierarchical Metamaterial for Broadband Microwave Absorption with Multi-scale Optimization and Integrated Design. *Compos. Sci. Technol.* 228, 109643(2022).

45. Qin, J. et al. Ultrabroadband and> 93% Microwave Absorption Enabled by "Doped" Water Meta-Atom Lattice with Subwavelength Thickness. *Adv. Mater.* **36**, 2411153 (2024).

46. Lin, J. et al. Anion Injection in Dielectric Ecosystems to Construct Dual Built-in Electric Fields for Efficient Electromagnetic Response. *Adv. Funct. Mater.* 2505381 (2025).

Acknowledgements

This work was supported by the National Natural Science Foundation of China (No. 12327804, 52231007, T2321003, 22088101, 22405050), National Key Research Program of China (No.

2024YFA1208902, 2024YFA1408000, 2021YFA1200600), Science and Technology Commission of Shanghai Municipality (No. 24ZR1406400), and Shanghai Municipal Education Commission (No. 24KXZNA06).

Author Contributions Statement

L.R., X.Z., X.W., B.L. contributed equally to this work. R.C., L.W., and L.R. participated in conceptualization, experiments design, supervision, and manuscript writing. L.R., X.Z., B.L., C.Z., and C.L. performed materials synthesis and characterization, including SEM, TEM, STEM, DPC, hologram, XRD, XPS, and XAFS. L.R., L.W., Z.W., and G.C. carried out theoretical simulation, calculation and results interpretation. L. R., X.W., W.Y., and L.W. designed and conducted EM performance tests. All authors contributed to data analysis, discussion, and manuscript preparation.

Competing Interests Statement

The authors declare no competing interests.

Additional information

Supplementary Materials is available for this paper.

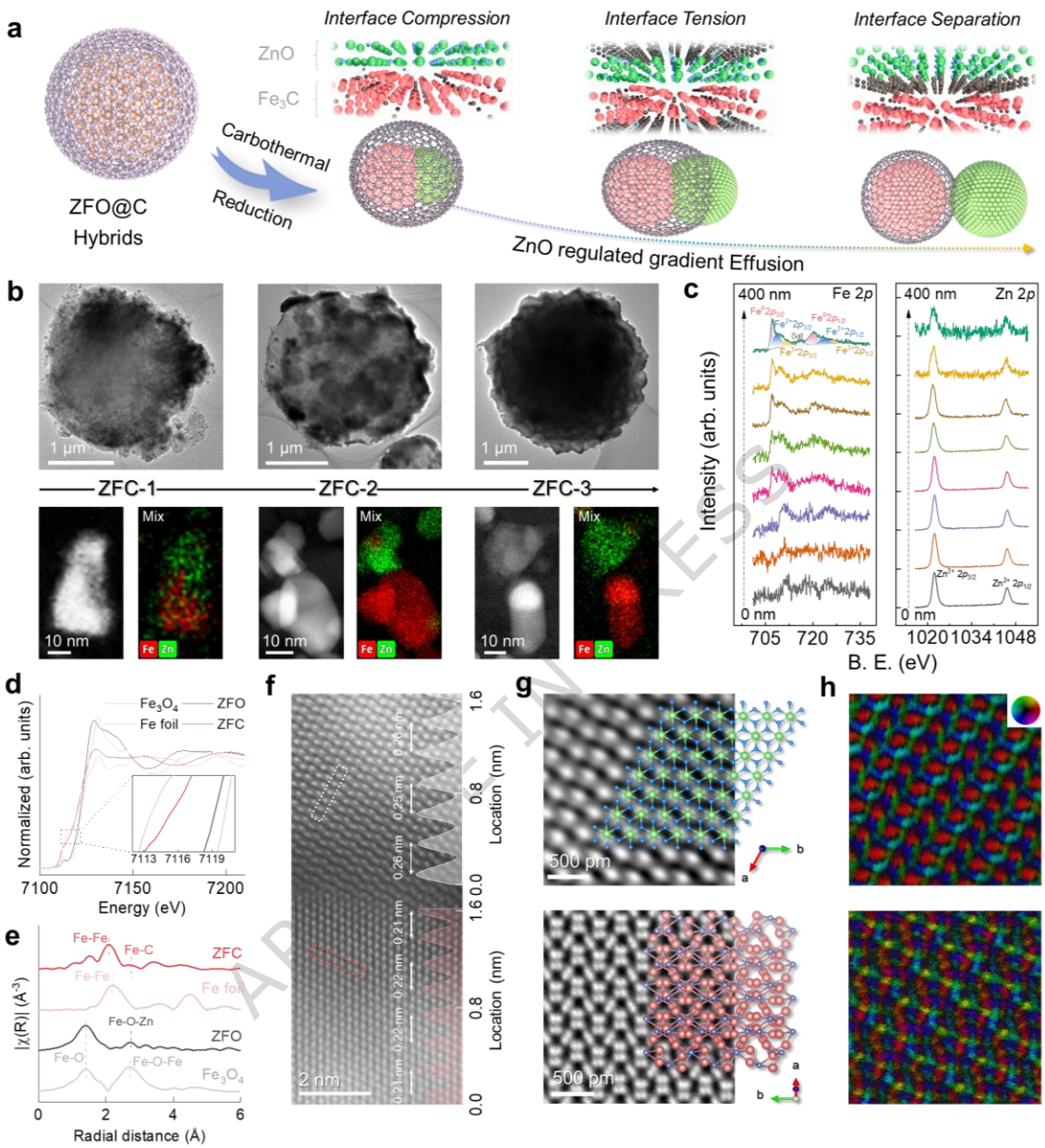

Figure 1 Synthesis and structure characterization. a Schematic illustration of ZnO diffusion tailored ZnO/Fe_3C heterostructures. **b** TEM images and HAADF-STEM elements mapping of the ZnO effusion affected ZnO/Fe_3C heterostructures. **c** XPS depth profiles identifying the distribution of ZnO and Fe_3C through the intensity variation of characteristic Fe 2*p* and Zn 2*p* signals. **d** XANES spectra at Fe *k*-edge, the inset is an enlarged peak. **e** EXAFS spectra at Fe *k*-edge. **f** Aberration-corrected atomic resolution STEM images of ZnO/Fe_3C magnetoelectric interface. **g** iDPC-STEM images of each component. **h** DPC images for visualizing the atomic-level polarized

electric field, the inset color wheel refers to the direction of the local electric field.

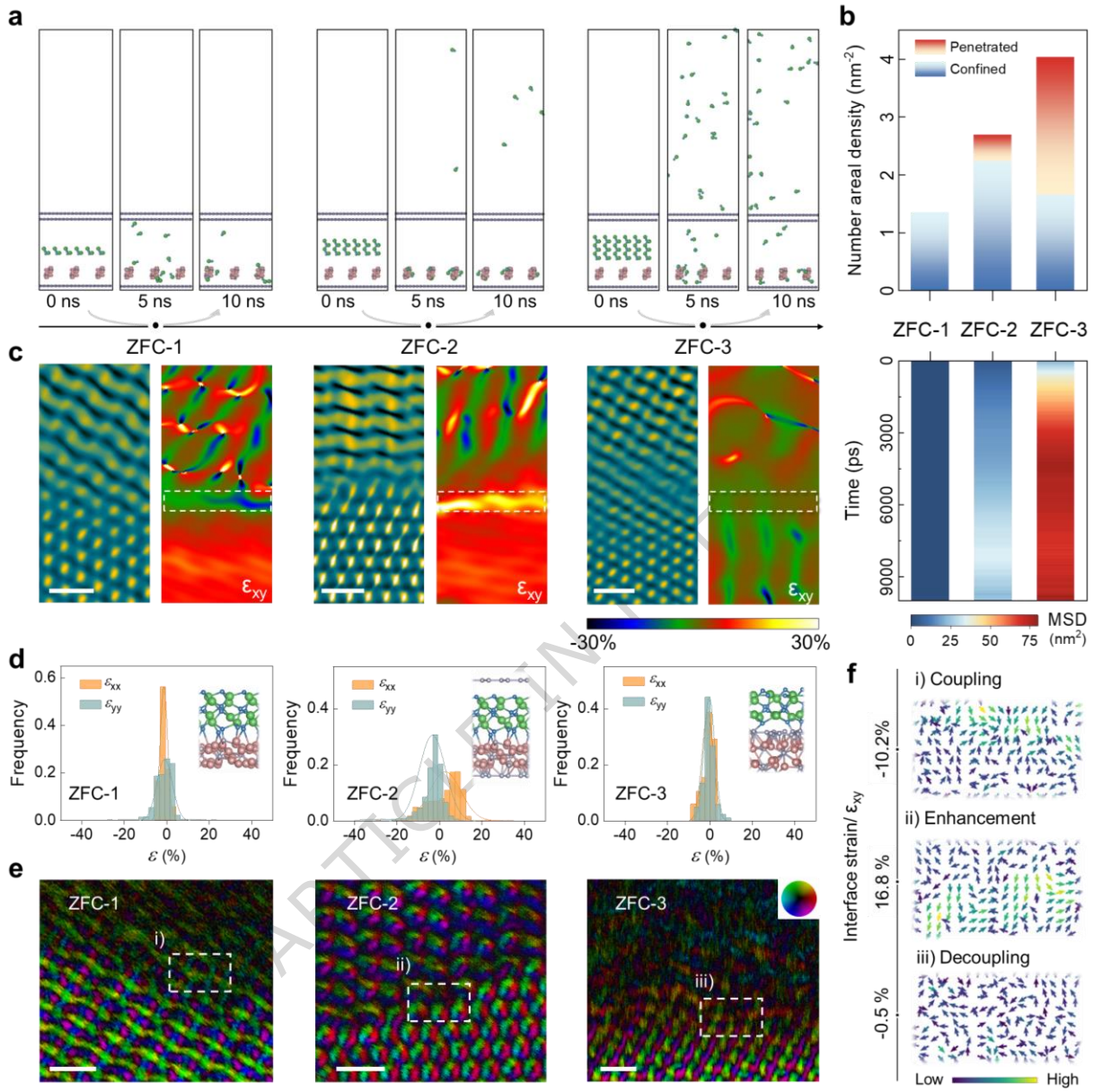

Figure 2 Effect of ZnO gradient diffusion on interface properties. a ZnO content affected gradient outward diffusion process resulted from molecular dynamics simulation. **b** Calculated number areal density of confined and penetrated ZnO and MSD variation along the time. **c** iDPC-STEM images of heterointerfaces and corresponding geometric phase analysis (GPA) results. **d** Statistical histograms of strain values illustrating the variability of interfacial strain. **e** Projected atomic electric field map of ZnO effusion reconstructed magnetoelectric interface. **f** Effect of interfacial strain on the vector field distribution of the selected region in e, the color bar

corresponds to the vector magnitude. All scale bars in **c** and **e** are 500 pm.

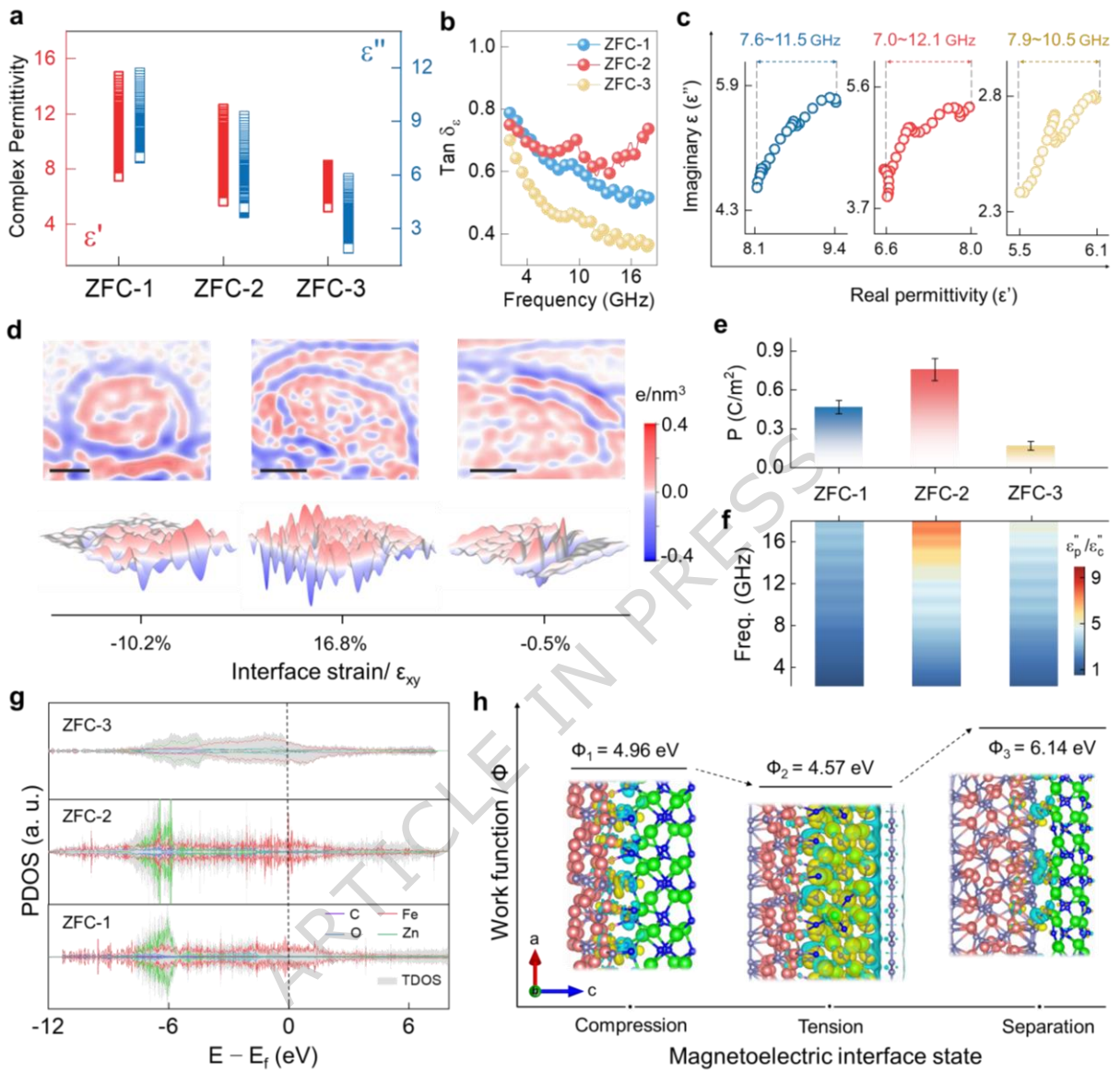

Figure 3 Dielectric properties and electronic structures. **a** Complex permittivity. **b** Tangent values of dielectric loss. **c** Cole-Cole plots over the frequency region corresponding to the strongest dielectric relaxation peaks. **d** Reconstructed electronic hologram and corresponding 3D charge density distribution images. **e** Calculated polarizability and **f** frequency dependence of $\varepsilon_p''/\varepsilon_c''$ ratio in ZFC-x. **g** Projected density of states (PDOS) of ZnO-diffusion reconstructed interfaces. **h** Calculated work function (Φ) values and charge density differences of ZnO diffusion reconstructed magnetoelectric heterostructure.

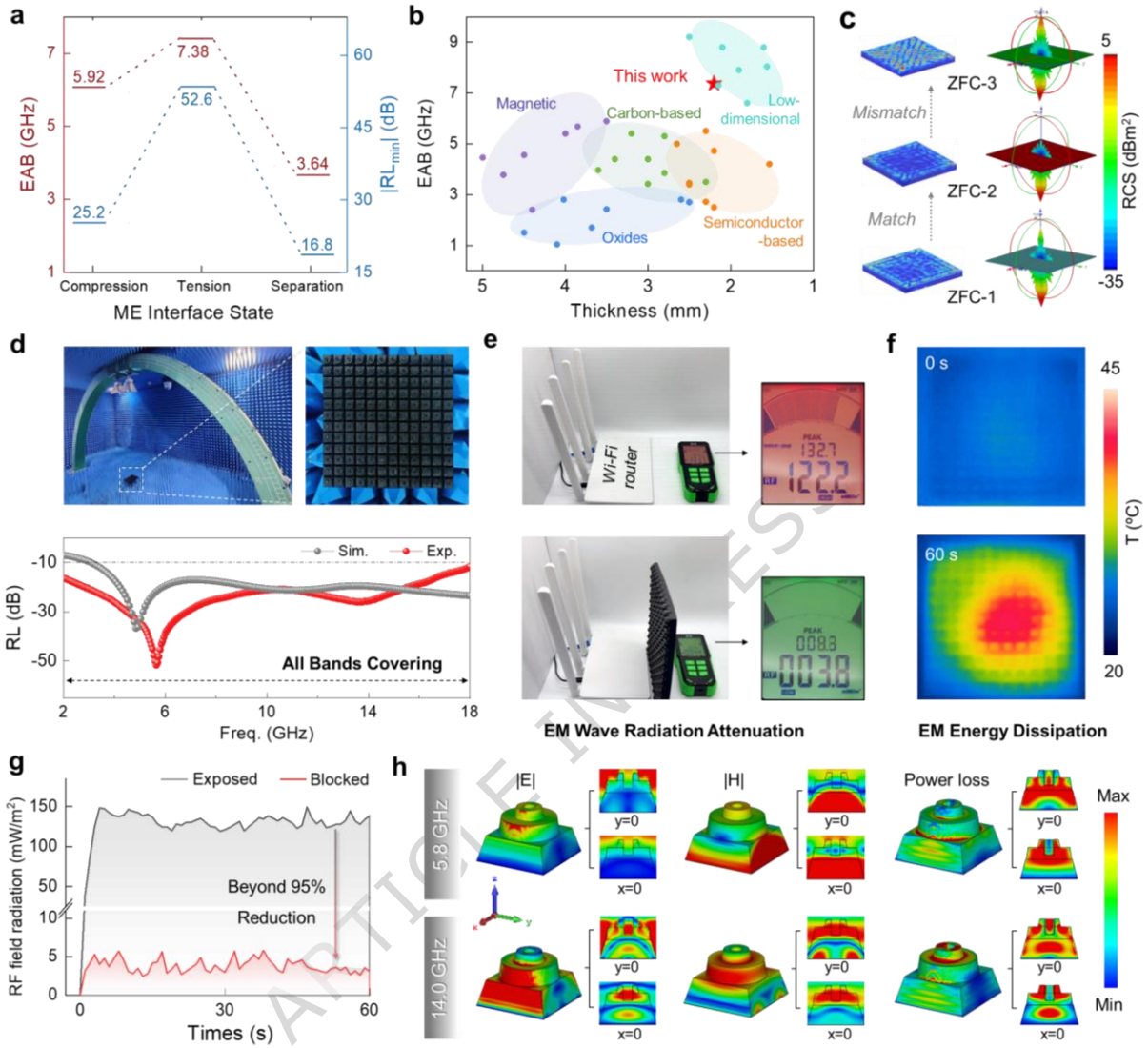

Figure 4 EM wave absorption performance. **a** EAB and $|RL_{min}|$ values of ZFC-x samples. **b** EAB properties comparison. **c** Surface current and 3D RCS simulation results of ZFC-x systems. **d** Digital photo of the ZFC-based metamaterial under the arch method testing environment and the corresponding RL results. **e** Photographs of EM signals detection without/with metamaterial blocking in front of a WiFi router. **f** Infrared thermal images of ZFC metamaterials before and after radiation under a solid-state microwave source. **g** RF-field radiation signals before and after applying ZFC-2 based metamaterials. **h** Finite element simulated electric field, magnetic field and power loss distribution of structure unit under 5.8 GHz and 14.0 GHz.

Editor's summary:
Authors propose an oriented diffusion strategy to design interfacial strain controlled magnetoelectric heterostructure, realizing the modulation of interfacial strain polarization coupling for enhancing electromagnetic absorption.

Peer review information: *Nature Communications* thanks Souvik Bhattacharjee, Anupam Gorai, Alexander V. Melentev and the other anonymous reviewer(s) for their contribution to the peer review of this work. A peer review file is available.